

# Investigation of Transverse Jet Injections in a Supersonic Crossflow Using Fast Responding Pressure-Sensitive Paint

Jim Crafton<sup>1</sup>, Alan Forlines<sup>1</sup>, Steve Palluconi<sup>1</sup>, and Kuang-Yu Hsu<sup>1</sup>  
*Innovative Scientific Solutions, Inc., Dayton, Ohio*

Campbell Carter<sup>2</sup> and Mark Gruber<sup>2</sup>  
*Air Force Research Laboratory, Wright-Patterson AFB, Ohio*

**Traditional Pressure-Sensitive Paint (PSP) systems can provide data with high spatial resolution; however, the bandwidth is limited to a few Hz by the response time of the paint. Fast responding paints have demonstrated response times of up to 100 kHz. Ultra-bright LEDs and fast framing cameras combined with a porous polymer PSP can be used to produce a system capable of both high spatial resolution and high temporal bandwidth. Measurements of mean and unsteady pressure have been acquired on an experimental setup composed of a Mach-2 channel flow with transverse jet injection. The unsteady pressure data clearly resolves structures not present in the mean pressure data, including multiple lambda shocks upstream of a strong bow shock, high frequency perturbations in the location of these shocks, and significant deformations of the bow shock structure. Time series of data can be extracted at each pixel and the spectral content and phase relationship of the flow can be presented as maps of pressure fluctuations at specific frequencies or as correlation coefficients between a control point and the remaining flow. This types of map can be created using arrays of fast pressure transducers; here, we present data representing an array of over 26,000 fast pressure transducers.**

## I. Introduction

There is a strong need for quantitative experimental data for CFD model development and validation. Furthermore, time-resolved computations of high-speed flowfields using the Large-Eddy Simulation (LES) technique are now becoming more common<sup>1 2 3 4</sup>, and thus there is also an interest in high-temporal-bandwidth measurements. The jet-in-crossflow is a simple configuration and as such is often considered a canonical problem for both low- and high-speed flows. For high-speed flows, it has many interesting features that make it challenging to simulate, including flow separation (both upstream and downstream of the jet axis) and unsteadiness; furthermore, the degree of separation and unsteadiness appear to depend strongly on injection angle and pressure. This data set is thus intended to augment a series of measurements characterizing the injection of a jet into a Mach-2 crossflow<sup>5</sup> and to provide modelers with high fidelity data for validation purposes of advanced computational models.

The measurement of unsteady pressures can be difficult because of the logistics of installing unsteady pressure transducers. The cost of installing a significant number of transducers can be prohibitive and, in some cases, impossible because of thin sections or moving/morphing control surfaces. Furthermore, data are available only at discrete points when using taps. The investigation of unsteady flows would be facilitated by a system that could acquire pressure with high spatial resolution and high temporal bandwidth in a non-intrusive manner. Pressure-Sensitive Paint<sup>6</sup> (PSP) is an image-based technology that has been used for continuous measurements of pressure on aerodynamic surfaces. The measurement is accomplished by applying the paint to the surface of interest and illuminating the surface with blue or UV radiation to excite the dye within the paint. The surface is imaged through a filter that isolates the excitation light from the pressure sensitive luminescence of the paint. Each pixel on the camera acts as a pressure *tap*, and therefore, continuous distributions of the pressure on the painted surface are acquired.

---

<sup>1</sup> Research Scientist, Innovative Scientific Solutions Inc.

<sup>2</sup> Principal Aerospace Engineer, Air Force Research Laboratory

## II. Experimental Approach

PSP offers non-intrusive pressure measurements with high spatial resolution; however, standard paints only produce mean pressures as their response times are on the order of 1 s. Fast responding PSP<sup>7</sup> formulations for unsteady pressure measurements have been developed. These formulations include anodized aluminum and porous polymer paints that have demonstrated bandwidths of up to 100 kHz (i.e., response times of  $\sim 10$   $\mu$ s). The experimental community has envisioned combining these fast PSPs with fast framing digital cameras and ultra-bright illumination sources to produce a system that acquires millions of data points at speeds of several kHz. The resulting system would act as an array of fast pressure transducers. The data produced by this system could be analyzed to provide frequency content of the flow at each spatial location. Unfortunately, older PSP illumination sources and fast framing cameras, combined with earlier fast PSP formulations, do not produce sufficient signal to perform quantitative fast PSP measurements.

Over the past few years, ultra-bright LEDs and fast-framing CMOS (complementary metal-oxide semiconductor) cameras have been developed that can significantly improve the performance of the fast PSP systems. The optical power from modern LEDs has increased by 100 times in less than 10 years. Newer fast framing CMOS chips operate with lower read noise than older models and the quantum efficiency for visible radiation is reasonably high ( $> 30\%$ ). In this study, we have combined an ultra-bright LED illumination source with a fast framing CMOS camera and a PtTFPP-based porous polymer paint to produce a high-temporal-bandwidth, high-spatial-resolution PSP system. This system was used to measure surface pressure around a wall injector in a Mach-2 crossflow. Mean pressure measurements were acquired on the channel wall near the jet using a binary PSP system. The fast PSP system was used to acquire data at frame rates of 7 kHz, using the full camera array (1k $\times$ 1k), and 25-kHz data was acquired at reduced spatial resolution. The experimental setup and results are described following a brief overview of “conventional” and fast PSP technologies.

### A. Pressure-Sensitive Paint

A typical PSP<sup>6</sup> is composed of an oxygen-sensitive fluorescent molecule and an oxygen permeable binder. The PSP method is based on the sensitivity of certain luminescent molecules to the presence of oxygen. When a luminescent molecule absorbs a photon, it transitions to an excited singlet energy state. The molecule then typically recovers to the ground state by the emission of a photon of a longer wavelength. In some materials oxygen can interact with the molecule such that the transition to the ground state is non-radiative; this process is known as oxygen quenching. The rate at which these two processes compete is dependent on the partial pressure of oxygen, with a higher oxygen partial pressure resulting in a higher rate of quenching and thus a lower intensity of luminescence.

Image-based pressure measurements using PSP are accomplished by coating the model surface with the paint and illuminating the surface with radiation of the appropriate wavelength to excite the luminescent molecule. The surface is imaged through a long-pass filter to separate the luminescence from the excitation light. A schematic of a typical system is shown in Figure 1. Unfortunately, the luminescence from the paint is not only a function of pressure but instead varies with illumination intensity, probe concentration, paint layer thickness, and detector sensitivity. These spatial variations result in a non-uniform signal from the painted surface. The spatial variations are eliminated by taking the ratio of the luminescent intensity of the paint at an unknown test condition,  $I$ , with the luminescent intensity of the paint at a known reference condition,  $I_o$ . Using this *wind-on/wind-off* ratio, the response of the system can be modeled using a *modified* Stern-Volmer equation:

$$\frac{I_o}{I} = A(T) + B(T) \frac{P}{P_o} \quad (1)$$

where  $T$  is the temperature and  $P$  and  $P_o$  are the respective *wind-on* and *wind-off* pressures. This approach is commonly known as Radiometric PSP.

Sources of uncertainty for PSP measurements have been investigated and modeled by Liu and Sullivan<sup>6</sup>. These error sources include temperature, illumination intensity, model displacement and deformation, sedimentation, photo-degradation, and camera shot noise. Liu and Sullivan concluded that the major sources of error for most PSP tests are related to illumination and temperature. The relationship between surface illumination and paint luminescence is linear; therefore, any change in surface illumination will result in an equal change in paint luminescence. Generally, this change in surface illumination is the result of model movement between the wind-off and wind-on images. As the model changes position, the distance between any point on the airfoil surface and the fixed PSP lighting will vary. The relationship between illumination intensity at a point on the surface and the distance between the PSP lighting

and the point of interest are an inverse function of the distance squared. The result is an error in the PSP measurement that is a function of the model movement. This error, however, can be eliminated by using a Binary PSP.

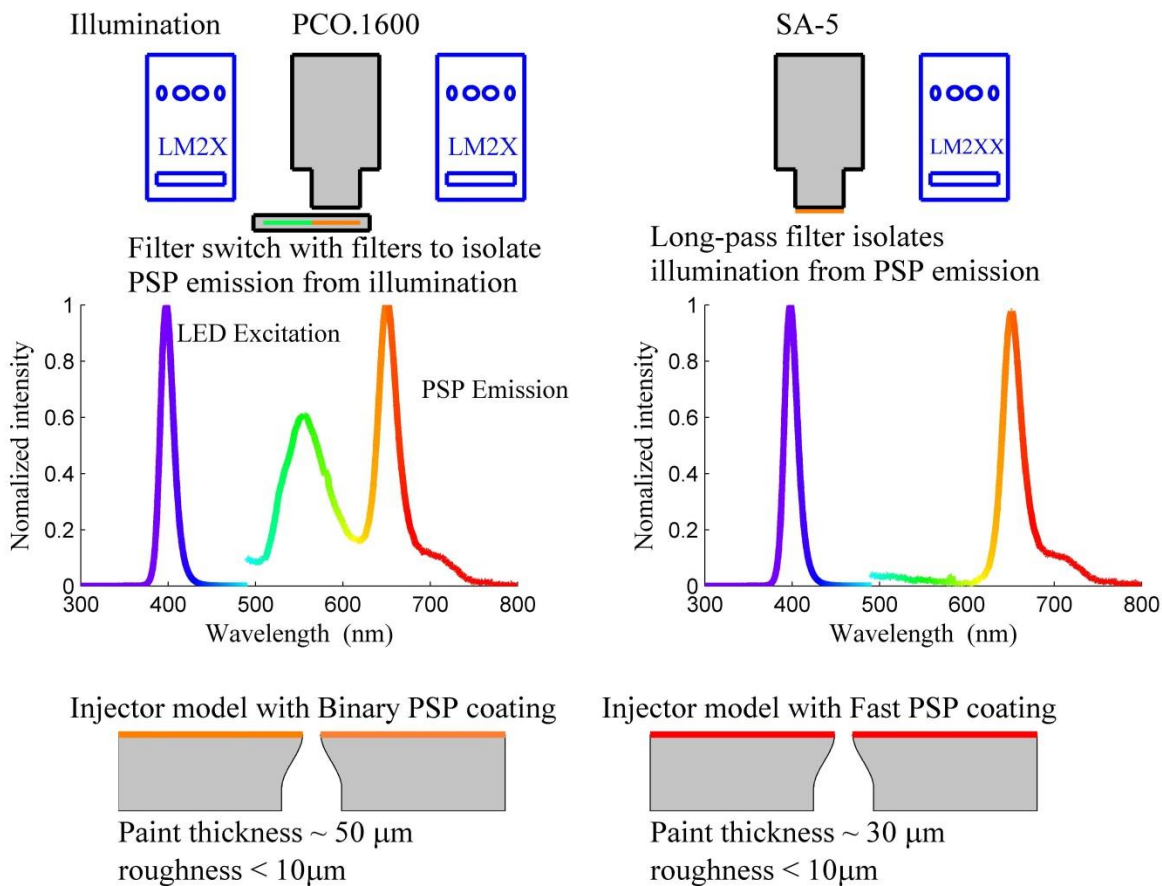


**Figure 1: Schematic of the experimental setup for binary (left) and fast (right) PSP.**

A Binary PSP includes a *reference probe* to minimize/eliminate illumination errors<sup>8,9</sup>. The goal is to use the luminescence of the reference probe to correct for variations in the luminescence of the signal probe (the pressure sensor) that is caused by variations in illumination. This is accomplished by taking a ratio of the luminescence of the signal probe to the luminescence of the reference probe. Since the luminescent signal from each probe is a linear function of the illuminations, the ratio of the signals from the probes naturally eliminates illumination variations from the equation. Innovative Scientific Solutions, Inc. (ISSI) has developed a binary paint based on Platinum tetra(pentafluorophenyl)porphine (PtTFPP) in Fluoro/Isopropyl/Butyl (FIB) with a temperature sensitive reference probe. The resulting binary FIB<sup>10</sup> paint has very low temperature sensitivity, and therefore, minimizes the second major source of error identified by Liu and Sullivan while compensating for illumination errors.

### **B. Fast Responding Pressure-Sensitive Paint**

Typical paint formulations are comprised of an oxygen-sensitive fluorescent dye and a binder for physically attaching the dye to the model surface. Conventional formulations typically use a polymer as a binder material. The disadvantage of the binder is that it inhibits the interaction of the atmospheric oxygen and the embedded dye molecules. The response time of the paint to pressure is largely governed by the rate of diffusion of gas within the binder. Conventional, polymer-based paint formulations have response times on the order of 1 s, making them unsuitable for evaluating unsteady aerodynamic phenomena such as unsteady flows, acoustics, or aeroelastic phenomena.

The temporal-response characteristics of PSP are primarily governed by the thickness of the paint formulation and the diffusion coefficient of the binder material, according to the relation

$$\tau_{diff} \propto \frac{h^2}{D_m} \quad (2)$$

where the response time due to diffusion ( $\tau_{diff}$ ) increases with the paint thickness ( $h$ ) squared and decreases with increasing diffusion coefficient ( $D_m$ ). Some investigators have focused on decreasing the thickness of the paint in order to improve the response characteristics. This approach, however, has the disadvantage of sacrificing luminescent output from the paint and, thus, the signal-to-noise ratio (SNR). The paint formulation to be used in the proposed work has been developed based on the strategy of increasing the diffusivity of gas within the paint binder, as described by Gregory et al.<sup>7</sup> Porous binders have been developed with the goal of enhancing the oxygen diffusion within the paint layer and, thus, improving the temporal response.

The difference between a conventional polymer-based PSP and a porous PSP is described schematically in Figure 2. For conventional PSP, oxygen molecules in a test gas must permeate into the binder layer for oxygen quenching. The process of oxygen permeation in a polymer binder layer produces slow response for a conventional PSP. On the other hand, the dye in a porous PSP is open to the test gas so that the oxygen molecules are free to interact with the dye. The open binder creates a PSP that responds very quickly to changes in oxygen number density and, therefore, pressure. A large effective surface area due to the porous surface improves luminescence intensity; thus, a higher SNR can be achieved. The drawback of the porous PSP approach is that the dye is too accessible to the oxygen. This results in near-complete quenching of all of the dye molecules at very low pressures. These formulations are effective for supersonic tunnels where the static pressure is below 20 kPa. For flows with higher pressures, the SNR ratio suffers.

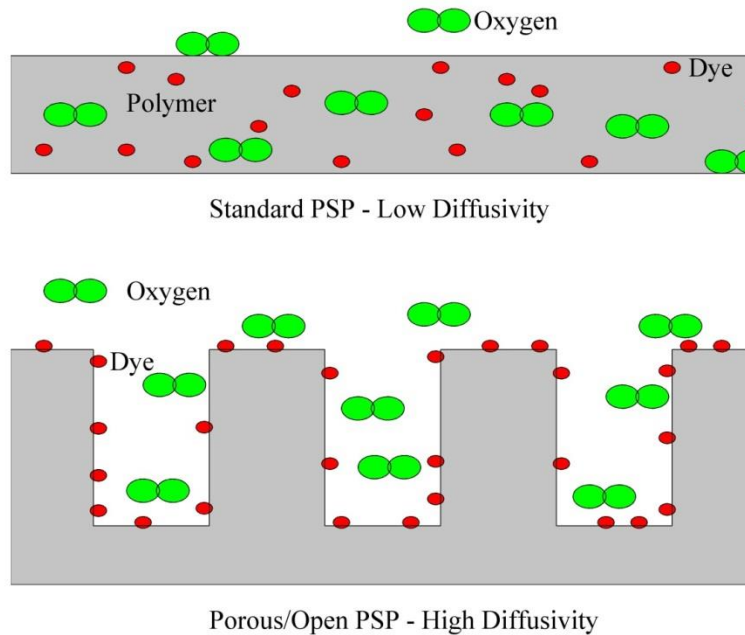


**Figure 2: Comparison of conventional PSP (top) and porous PSP (bottom).**

Polymer/ceramic PSP<sup>11</sup> has been developed as a hybrid paint formulation that incorporates the advantages of both traditional and porous PSP. The polymer/ceramic formulation incorporates a high percentage of ceramic particles that provide the porous structure for rapid oxygen quenching with a small amount of polymer to bind the paint to the surface. A dye is deposited onto the polymer/ceramic surface to complete the paint formulation. The resulting system is a fast-time-response paint layer with favorable SNR at higher pressure. Unlike anodized aluminum the polymer based paint can be air brushed onto a model; thus, paint application to complex surfaces is possible.

Experimental demonstrations of fast PSP have been conducted by several research teams. Gregory and Sullivan<sup>12</sup> have used these polymer/ceramic PSP formulations to measure oscillating pressure fluctuations with frequencies up to 20-kHz on a fluidic oscillator. Oscillating airfoils have been investigated by Fonov et al.<sup>13</sup> using a thin coating of a binary PSP. In this experiment, the pressure distribution on a NACA-0012 oscillated at 20-Hz was investigated, thus demonstrating the capability of fast PSP in a periodic flow. Non-periodic PSP data were acquired by Kameda et al.<sup>14</sup> on a delta wing in a Mach-0.6 flow. Here, Kameda detected the oscillation frequency of shocks on the delta wing at up to 170-Hz using frequency analysis of the PSP images. Nakakita<sup>15</sup> demonstrated point-by-point frequency analysis of a fast PSP signal acquired on a cylinder in cross-flow.

These experiments demonstrate the potential of fast PSP as a tool for experimental studies and the evolution of the tool for wind tunnel settings. It is noted that the current experiments incorporate many of the concepts previously demonstrated such as high-speed data acquisition and frequency analysis of the signal. The contribution of this work is incorporating newer instrumentation (camera and illumination source) to improve SNR of the PSP system and then employing modern computer processing software to analyze these large data sets. The improved instrumentation allows the focus to be on fluid dynamics rather than on the tool development while computing power allows these large data arrays to be analyzed in a manner similar to small arrays of traditional fast pressure transducers. The resulting data provides both high temporal bandwidth and high spatial resolution maps of unsteady pressure phenomenon in the flow.

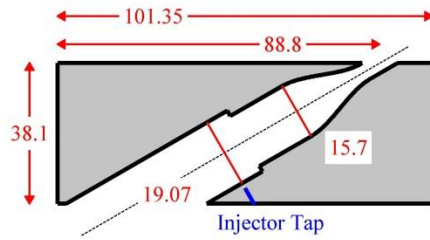
### C. Experimental Setup

The experimental study was conducted in a supersonic flow facility operated within the High-Speed Systems Division, of the Aerospace Systems Directorate, Wright-Patterson AFB (AFRL/RQH). A symmetric facility nozzle was used to produce supersonic flow at a nominal Mach number of 2. Schematics of the injector blocks tested are included in Figure 3. Four round injectors were employed: two injectors with 90° (normal) injection angle and two injectors inclined at an angle of 30° from the tunnel floor. Injector diameters were  $d_{inj} = 4.76$  and 7.94 mm, resulting in Reynolds numbers based on freestream conditions and nozzle diameter of 116,000 and 193,000. Previous measurements in this facility with these injector blocks using Raman scattering have characterized time-averaged injectant mole fractions<sup>5</sup>. This particular experiment is part of an ongoing effort to build a database for high-fidelity CFD model validation and development, not a fundamental jet in crossflow study.

The experimental setup for both binary and fast PSP measurements is composed of LED illumination sources, PSP, and a camera with a filter, similar to Figure 1. Optical access was provided by windows located on both the side walls and top wall of the test section. The binary PSP system was composed of a PCO-1600 CCD (charge-coupled device) camera with a 55-mm focal-length lens, a filter switch, two LM2X-400 LEDs, and a laptop PC running OMS Acquire. The fast PSP system utilized a Photron SA5 CMOS camera with a 50-mm focal-length lens. PSP was applied to the injector block surface, and data were acquired on each injector at injection pressures of  $P_{inj} = 117, 234, 351, 468,$  and 703 kPa; injection pressure was measured via a pressure tap within the injector block, as shown in Figure 3. It is noted that air was used as the injectant (rather than ethylene, as used in the study of Lin et al.<sup>5</sup>); an injectant other than air would create a bias in the pressure field derived from PSP. The wind tunnel stagnation pressure was  $P_0 = 234$  kPa and the stagnation temperature was 294 K. The corresponding jet-to-freestream momentum flux ratios for the above jet injection pressures were 0.5, 1.0, 1.5, 2.0 and 3.0.

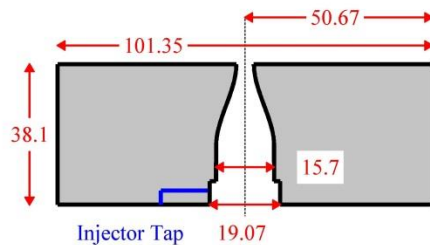
For the binary PSP dataset, 16-images each were acquired of the signal and reference probes at wind-off, injector-off, and each injector-on condition. The binary PSP data were processed and mapped onto a mesh of the injector block surface. For the fast PSP measurements, between 1,000 and 5,000 images were acquired at wind-off, injector-off, and each injector-on condition. A majority of the data was acquired with the full frame (1024×1024 pixels) of the camera at 7,000 frames/s (fps). Several datasets were acquired at a lower frame size (512×512 pixels) at 25,000 fps; in both cases, the exposure time was equal to the reciprocal of the framing rate. The fast PSP data was also processed and mapped onto a mesh of the injector block surface.

Jet injected 30° to flow  
Flow from left to right

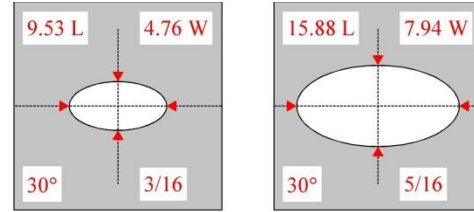


Side view of 4.76-mm 30° Nozzle

Dimensions in mm  
Jet injected 90° to flow



Front view of 4.76-mm 90° Nozzle



Detailed view of Nozzles

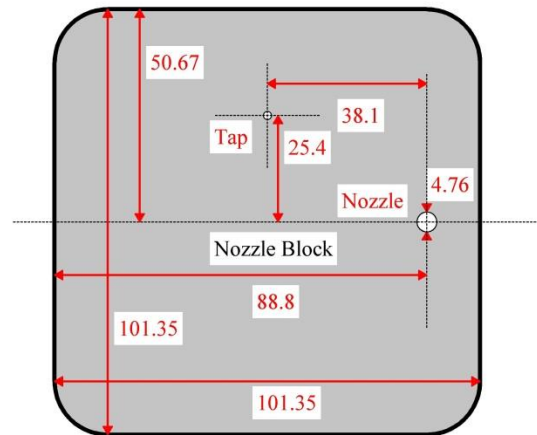
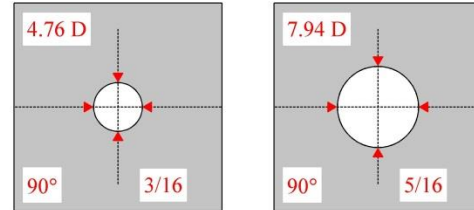


Figure 3: Schematic of injector blocks.

### III. Results

Data were first acquired using the binary FIB PSP system at each of the operating conditions. A single pressure tap (in the field of view) was used for an *in-situ* correction of the PSP data. Past experience in this facility indicates that the final binary PSP data should be accurate to within 200-Pa after the *in-situ* bias correction. The binary paint data is used to produce a mean pressure distribution, and as an *in-situ* validation of the calibration for the porous polymer. An example of the pressure distribution at  $P_{inj} = 234$ -kPa with the 4.76 mm normal injector block is shown in Figure 4. The flow features, such as the stagnation zone with high pressure just upstream of the jet, the bow shock upstream of the stagnation zone, and the low pressure region behind the injector are expected. The flow is very symmetric about the injector. The pressure rises slowly from the bow shock toward the injector. There is a small pressure decrease, associated with a horseshoe vortex, followed by a stagnation zone just upstream of the jet. The low pressure zone behind the injector is again symmetric, with the flow expanding to return to a flat pressure distribution downstream of the injector. Behind the jet, there are expansion fans emanating from the low- pressure zone.

An example of the same injector block operated at a lower and higher injection pressure is shown in Figure 5 and Figure 6, respectively. The overall structure of the flow is unchanged. The bow shock, horseshoe vortex, and stagnation zone are still present in front of the jet. The horseshoe vortex is not clearly defined at the lowest injector pressure. There is still a low pressure zone behind the jet. As the injector pressure increases, the bow shock moves upstream, and the stagnation pressure in front of the jet increases. The low-pressure zone and expansion fans behind the jet are also expanding and extending downstream. The location of the horseshoe vortex and the amplitude of the high-pressure zone in front of the jet are more evident in a plot of the pressure distribution through the centerline of the jet, shown in Figure 7. As injection pressure increases, the location of the high-pressure ridge and low-pressure trough in front of the jet move upstream, and the low pressure zone downstream of the jet expands.

The impact of injector geometry is demonstrated in Figure 8 and Figure 9 where the pressure distributions for the 7.94-mm-diameter 90° and 30° injector blocks with  $P_{inj}=468$ -kPa are displayed. The structure of the shock system is not dramatically modified by the 7.94-mm-diameter normal injector. The strength of the shock and maximum magnitude of the pressure in the stagnation zone are only slightly greater. The standoff distance and overall scale of the bow shock are increased with the larger diameter injector. The horseshoe vortex is still evident and the overall structure of the flow is consistent with the 4.76-mm injector.

The pressure distribution is significantly modified by the 30° injector, displayed in Figure 9. The magnitude of the pressure rise through the leading bow shock is similar to that of the normal injector; however, the strong stagnation zone upstream of the jet and the horseshoe vortex are no longer evident, and the bow shock does not extend upstream. The bow shock has a sharper nose, and the shock weakens more quickly away from the centerline in the case of the 30° injector. These features are evident in the pressure distribution along the centerline of the 90° and 30° injectors, which is plotted at three injection pressures in Figure 10. Finally, the low-pressure zone downstream of the injector is significantly smaller and narrower for the 30° injector. The overall effect of the normal injectors is similar to an obstacle in the flow such as a strut-endwall configuration. The flow stagnates and moves around the obstacle creating a bow shock, horseshoe vortex, and stagnation zone. The 30° injector behaves more like an angled strut or ramp. The flow is turned and modified by the obstacle, but the impact on the flow is less dramatic.

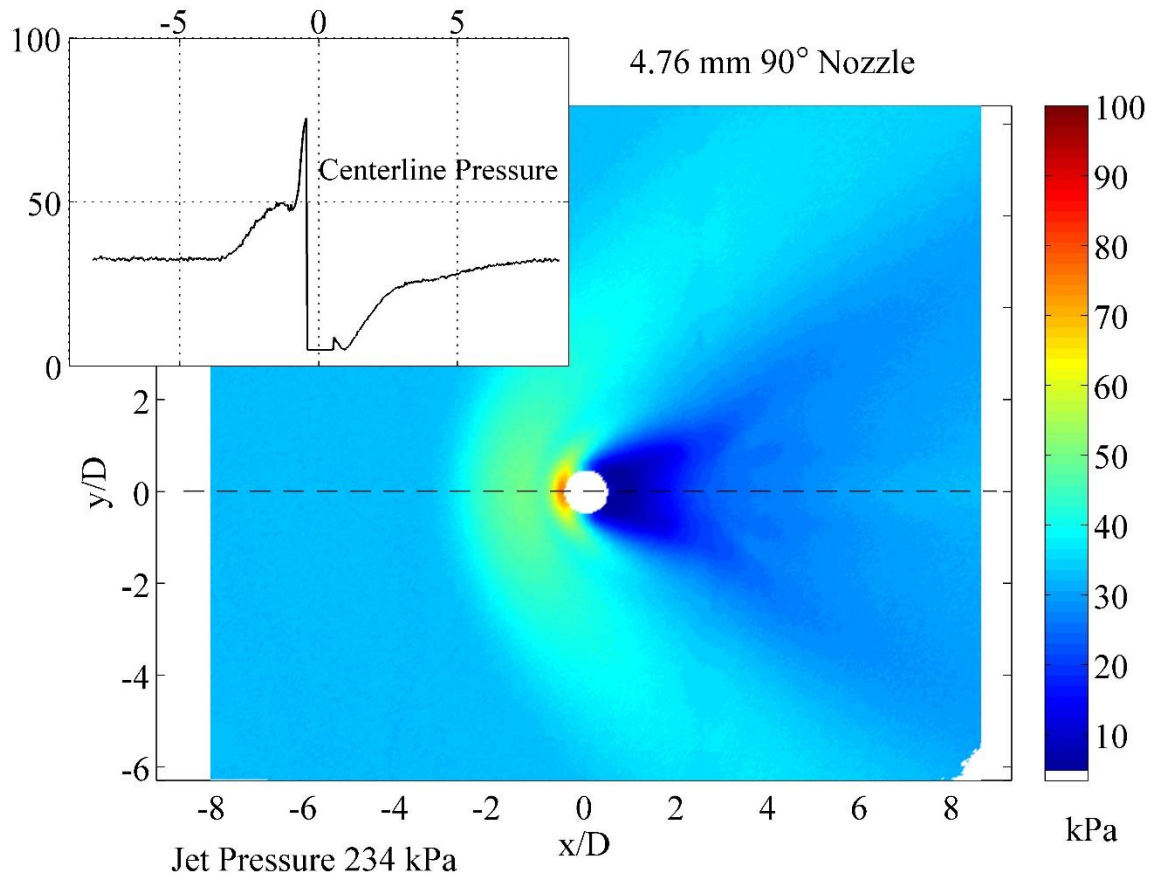


**Figure 4: Mean pressure distribution for 4.76-mm-diam., 90° injector block operating at  $P_{inj} = 234$ -kPa**

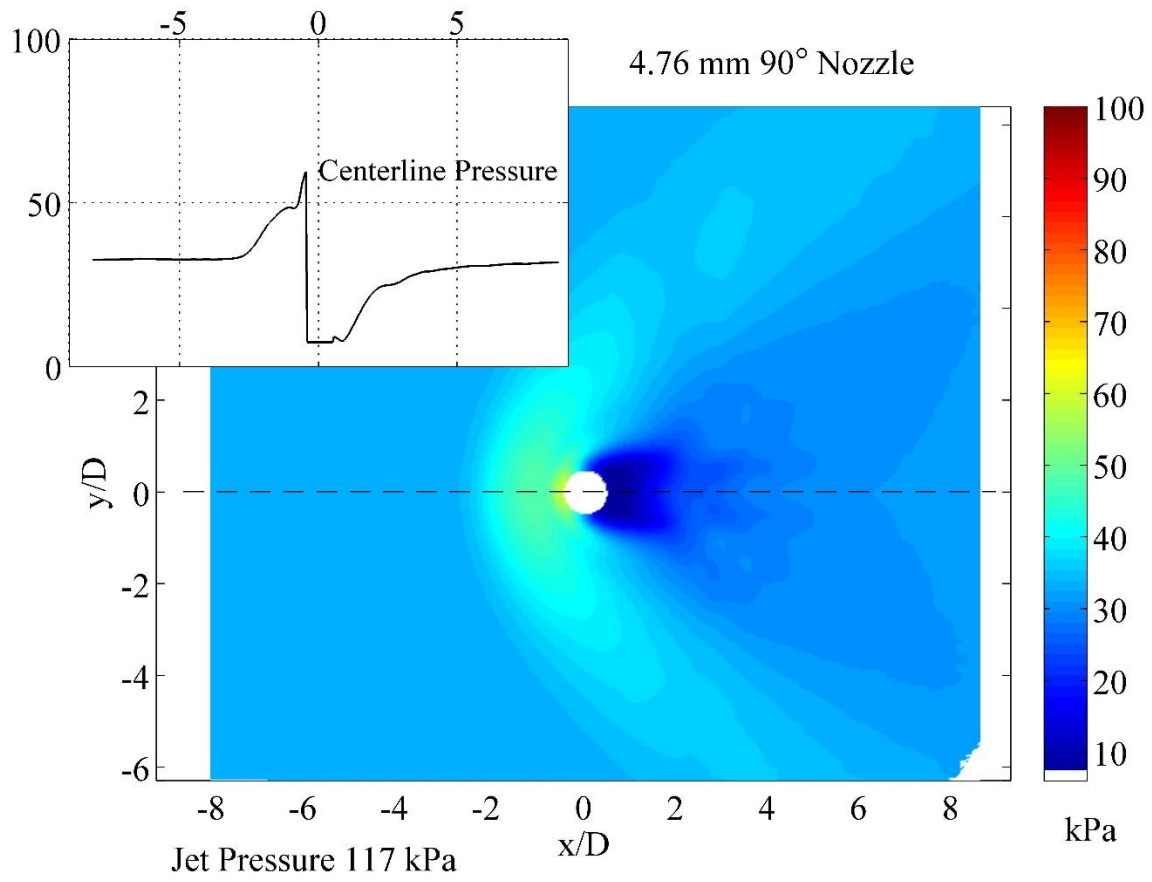


Figure 5: Mean pressure distribution for 4.76-mm-diam., 90° injector block operating at  $P_{inj} = 117$ -kPa

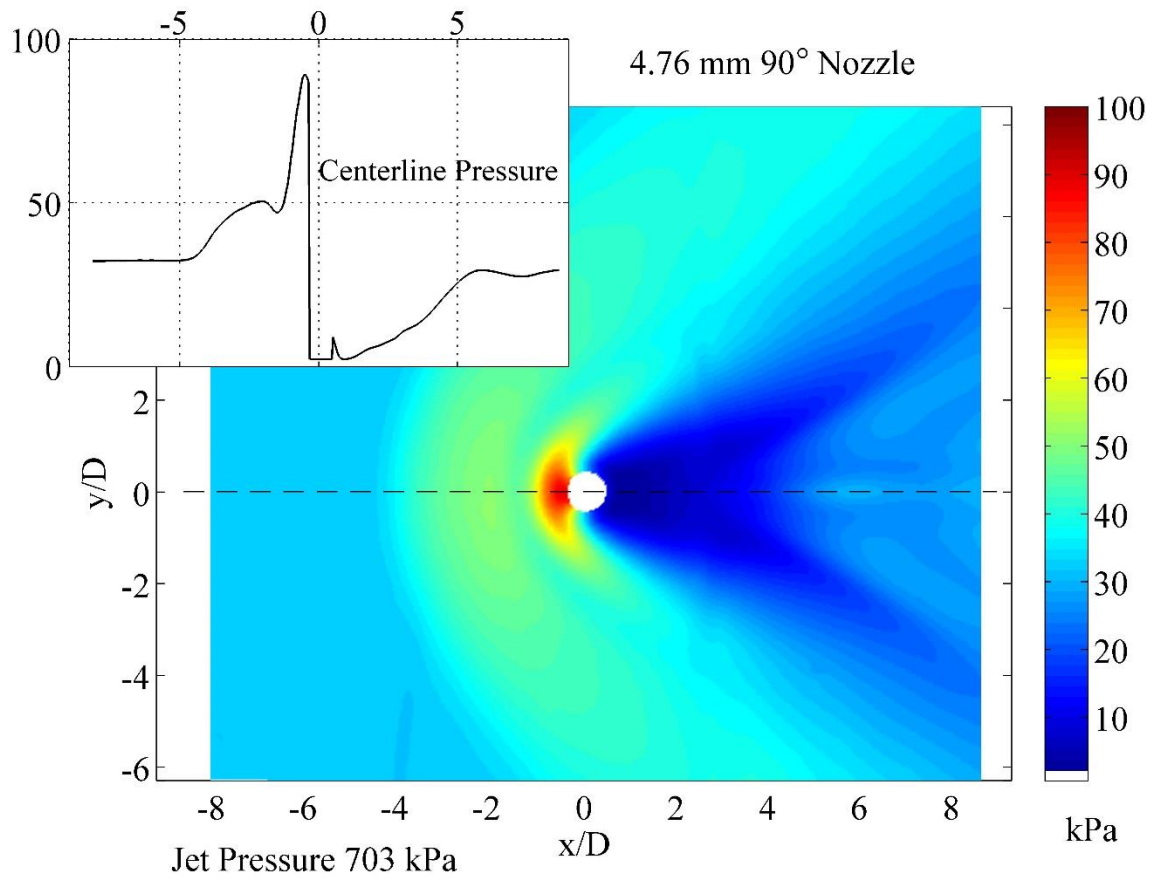
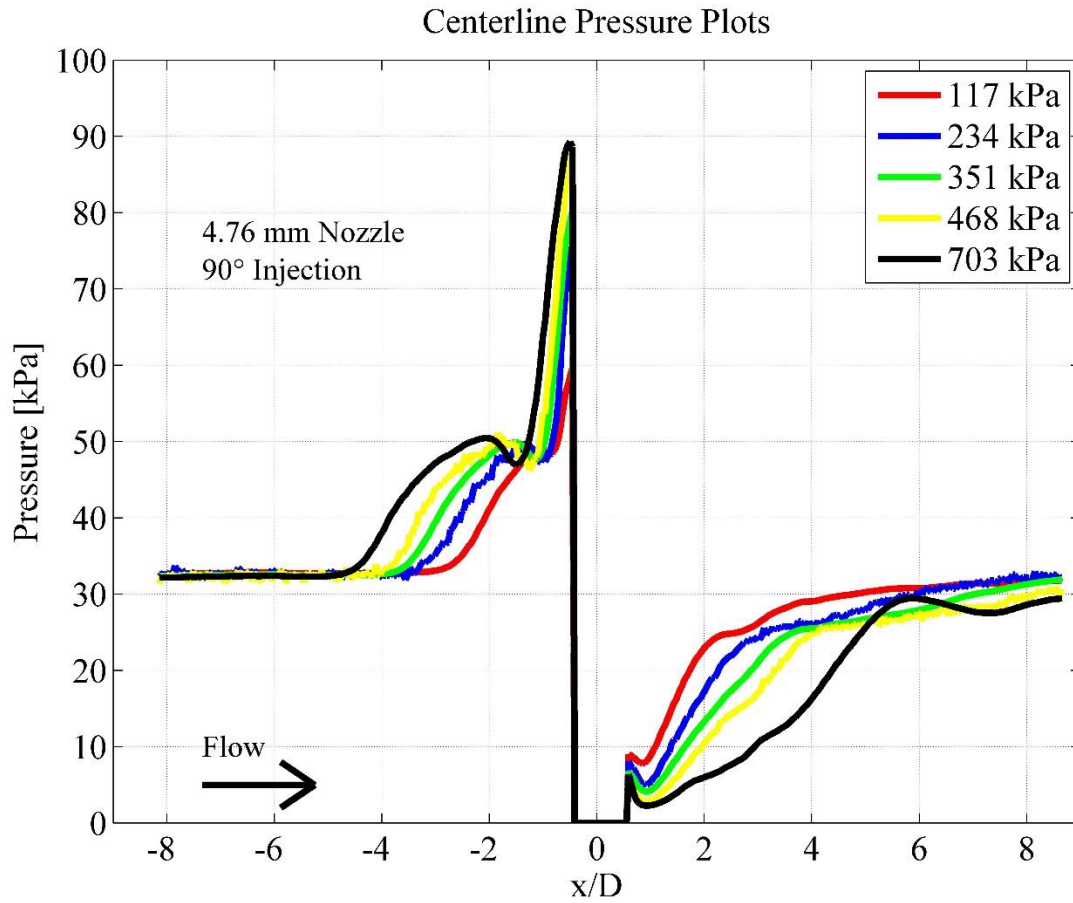


Figure 6: Mean pressure distribution for 4.76-mm-diam., 90° injector block operating at  $P_{inj} = 703$ -kPa



**Figure 7: Pressure distribution along centerline of 4.76–mm-diam., 90° injector block at several injection pressures**

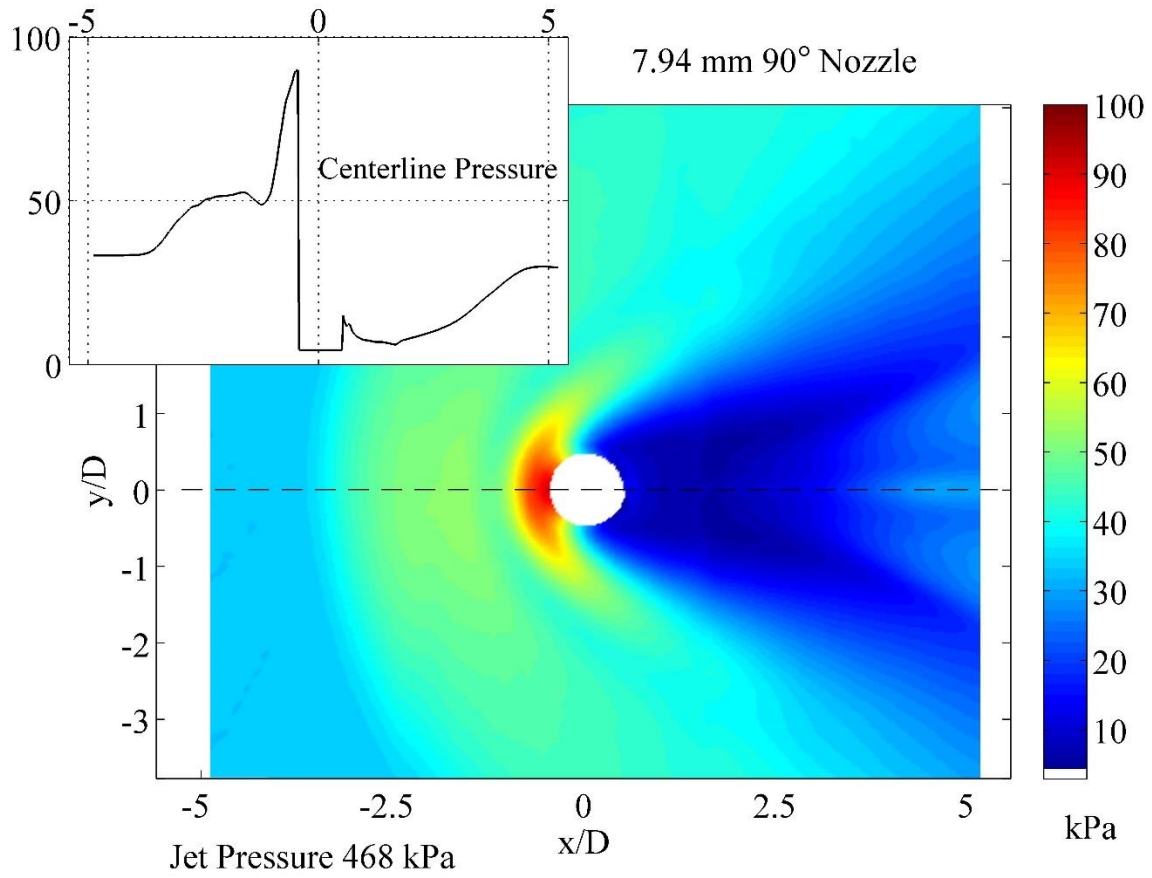


Figure 8: Mean pressure distribution for 7.94-mm-diam., 90° injector block operating at  $P_{inj} = 468$ -kPa

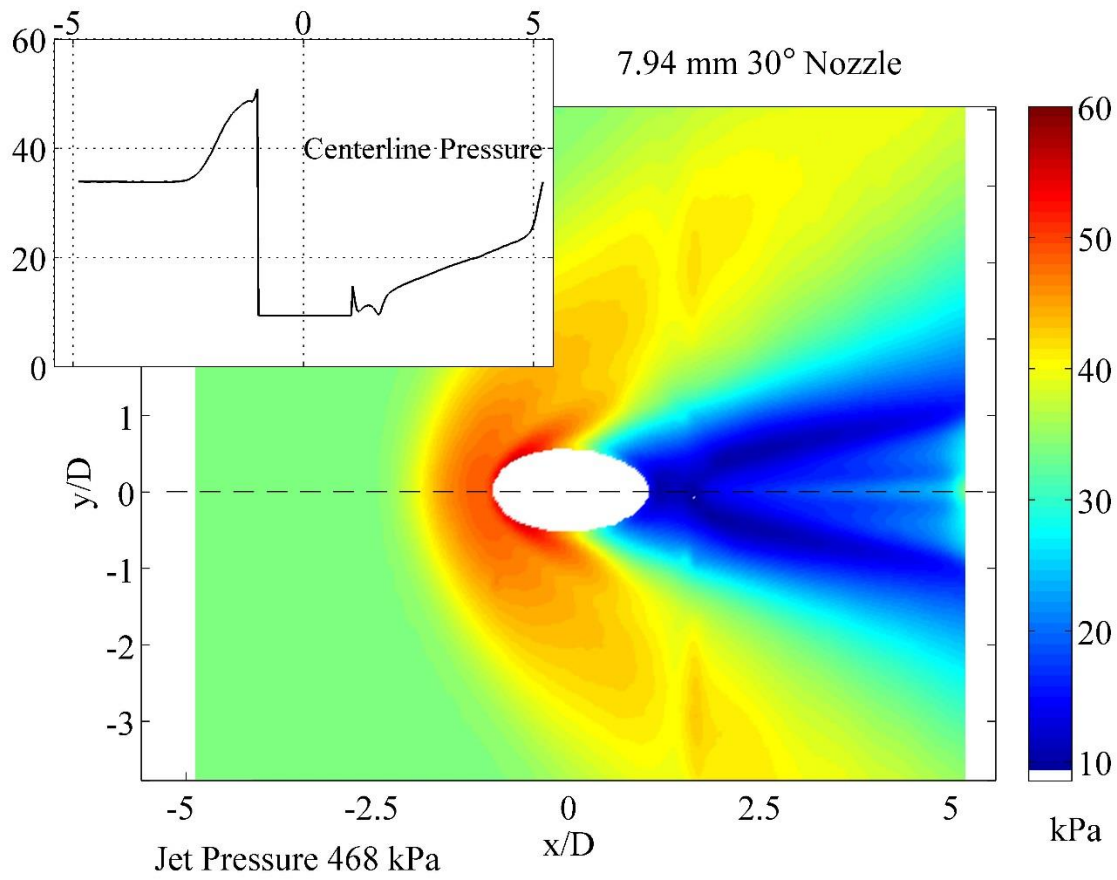
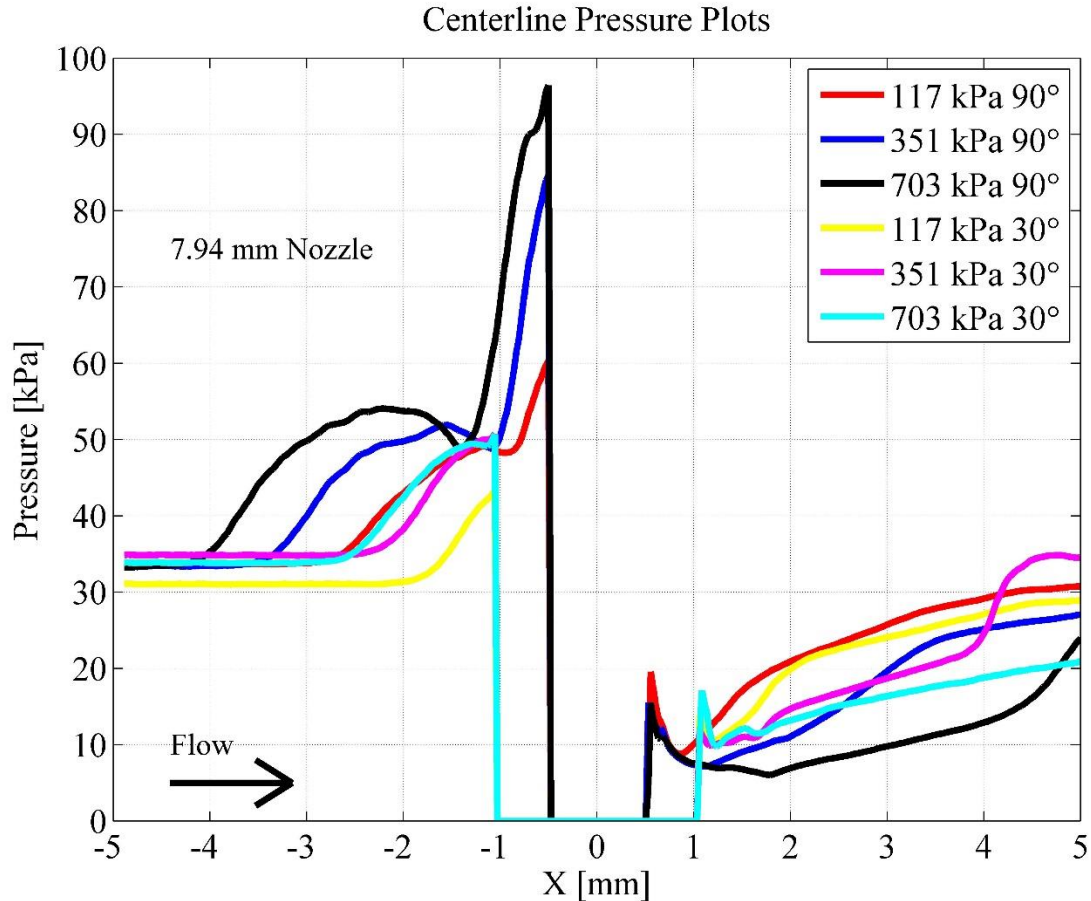


Figure 9: Mean pressure distribution for 7.94-mm-diam. 30° injector block operating at  $P_{inj} = 468$ -kPa



**Figure 10: Mean pressure distribution for 7.94-mm-diam., 90° and 30° injector block operating at several injection pressures**

The data presented in Figure 4 - Figure 10 were acquired using a traditional low-bandwidth PSP, and therefore, the pressure distributions represent the mean pressure. The unsteady pressure distribution was investigated by applying the porous polymer PSP to the surface, and the test series was repeated. At each test condition, a sequence of 1,000 frames was recorded at an exposure time of 140- $\mu$ s and a frame rate of 7,000 fps. The calibration of the porous polymer PSP is not as well established as binary FIB, and the temperature sensitivity of the paint is significantly higher. As there was only one pressure tap in each injector block, the binary FIB results were used to validate the calibration of the porous polymer paint.

The 1,000 frame sequence of images from the  $d_{inj} = 4.76$  mm 90° injector block with the fast paint data was averaged and processed to create a mean pressure distribution. The fast PSP data was processed using a paint calibration at several different temperatures. The resulting pressure data at several distinct locations (indicated in Figure 11) on the injector block from the fast paint are plotted versus the binary FIB paint data in Figure 11. Assuming the fast PSP and binary FIB PSP are in perfect agreement, the data should produce a curve with a slope of 1 and an intercept of 0. The linear least squares fit for each temperature is shown at the bottom of Figure 11. The data processed at 293 K, which is slightly lower than the tunnel stagnation temperature of 295 K, compares favorably with the binary FIB data. The remainder of the fast PSP data was processed using the porous polymer calibration at 293 K. The data in the region upstream of the bow shock was used to create a bias correction by comparing the averaged PSP results to the pressure-tap value. This correction was generally less than 1-kPa.

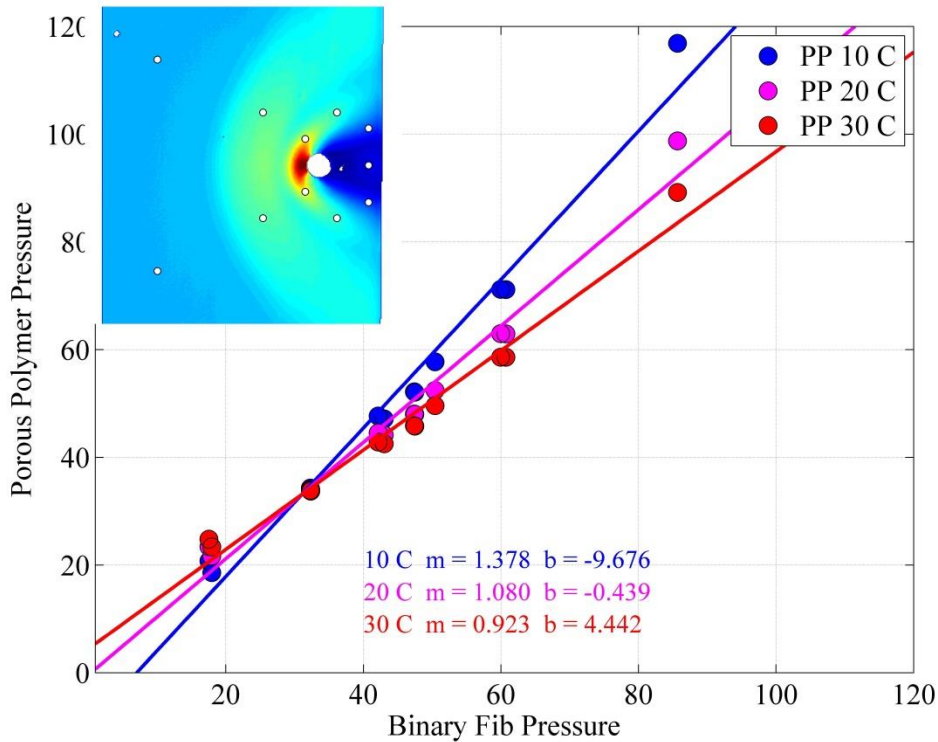


**Figure 11: Comparison of time averaged fast PSP and binary FIB data along the injector centerline**

It is noted that between the bow shock and the stagnation zone, the fast paint and FIB data do diverge by 4 to 5-kPa. One possible explanation for this deviation is a slight variation of the temperature in this region. The porous PSP is very sensitive to temperature, and therefore, temperature variations as small as 1-2 K could cause this level of error. The binary FIB, by comparison, has low temperature sensitivity. Further investigation of the flow may yield some insight into this disagreement between the binary FIB PSP and the porous polymer PSP data.

The fast PSP data from the 7.94-mm-diam., 90° injector block were processed, and an example of a sequence of images from the 703 kPa injection condition are shown in Figure 12. Here, the pressure distribution from the fast PSP is shown at eight time steps over a 2 ms period along with the mean pressure distribution. A comparison of the mean pressure distribution and the instantaneous pressure reveals several interesting features. The shape, position, and maximum pressure in the stagnation zone is quite dynamic. The high pressure ridge just in front of the jet moves side to side during the given sequence of images, is larger and stronger in some cases, (0 and 1714  $\mu$ s) weaker in a few cases, (857 and 1429  $\mu$ s) is offset to the side in some cases, (286 and 571  $\mu$ s) but rarely resembles the average. The shape and position of the bow shock is also quite dynamic. At the first several time steps, the bow shock is slightly asymmetric with a mild compression on the Y- side of the flow. It is also noted that there are several weak pressure ridges just upstream on the bow shock at several of the time steps. These weak pressure ridges were observed to fluctuate with the bow shock at many time steps. There are believed to be weak lambda shocks associated with the stronger bow shock. These lambda shocks are largely, but not completely, washed out of the mean pressure data.

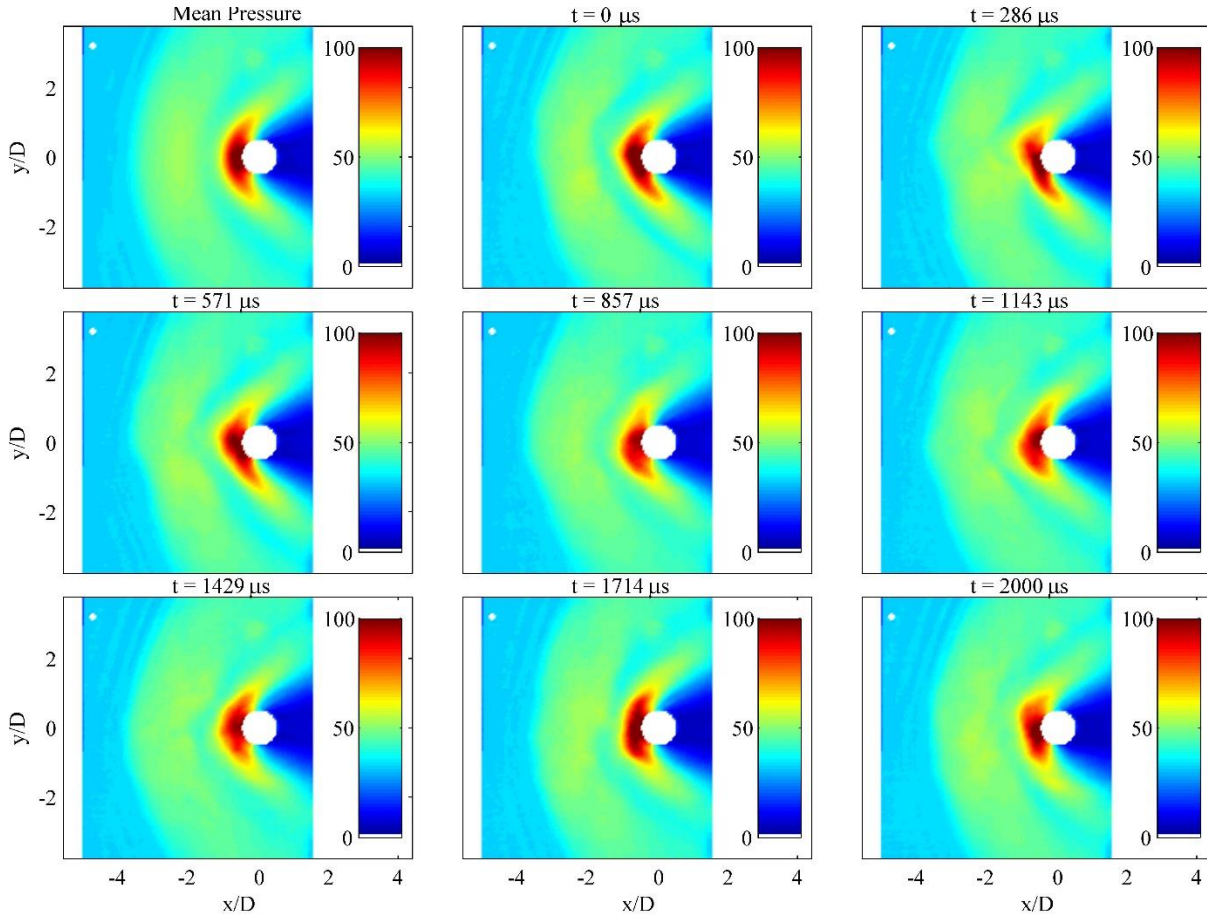


**Figure 12: Mean and instantaneous pressure distribution sequence for the 7.94-mm-diam., 90° injector block operating at  $P_{inj} = 703$ -kPa.**

The data presented in Figure 12 represents only a fraction of the potential of a fast PSP system. Using the fast PSP system, 2,000 samples similar to those in Figure 12 were acquired for this test condition. Furthermore, the data were acquired in a continuous stream at 7 kHz, and, therefore, can be presented and analyzed in a manner similar to traditional fast pressure tap data. The major advantage of the current system is that there are approximately 1 million transducers available for the analysis. Quantities such as the mean pressure (as shown in Figure 12) and amplitude of the pressure fluctuations at each spatial location can be computed.

The original fast PSP data set included over 1 million data points at 2,000 time steps. To mitigate the size of the data set, a 6-pixel low pass filter was applied to the data and the data was then mapped onto a 175 pixel by 150 pixel surface mesh. The resulting data set maintains a spatial resolution of 0.35 mm per pixel and represents an array of 26,000 fast pressure transducers. While some spatial resolution has been sacrificed, the binning filter does improve the SNR by a factor of 6, and the size of the data set is manageable for post processing. Fast PSP data can be extracted at each pixel and processed as unsteady pressure data. This process is demonstrated using the 4.76-mm-90° jet operating at 703-kPa.

The pressure history at four distinct locations (indicated in Figure 13) was extracted. The pressure in the freestream region, upstream of the bow shock, is nearly constant. Near the bow shock, the pressure fluctuates with an amplitude of several kPa. In the stagnation zone, the pressure fluctuations are similar to those near the bow shock, but the amplitude of the fluctuations is slightly higher. Behind the jet, the pressure drops, as does the amplitude of the fluctuations. This type of analysis can be repeated at each pixel, and a map of the amplitude of the pressure fluctuations can be generated. This analysis was performed on the data set and the pressure fluctuations were converted to Sound Pressure Level (SPL), the data is presented in Figure 13. The pressure fluctuations are largest in the stagnation zone where the amplitude is about 168 dB (5 kPa) but there is also a second region of large pressure fluctuations associated

with the bow shock, perhaps related to fluctuation in the strength or the location of the bow shock. A final set of large pressure fluctuations is present near the location of the horseshoe vortex and just upstream of the stagnation zone. These fluctuations have a magnitude of about 160 dB (2 kPa), similar to that in the bow shock.

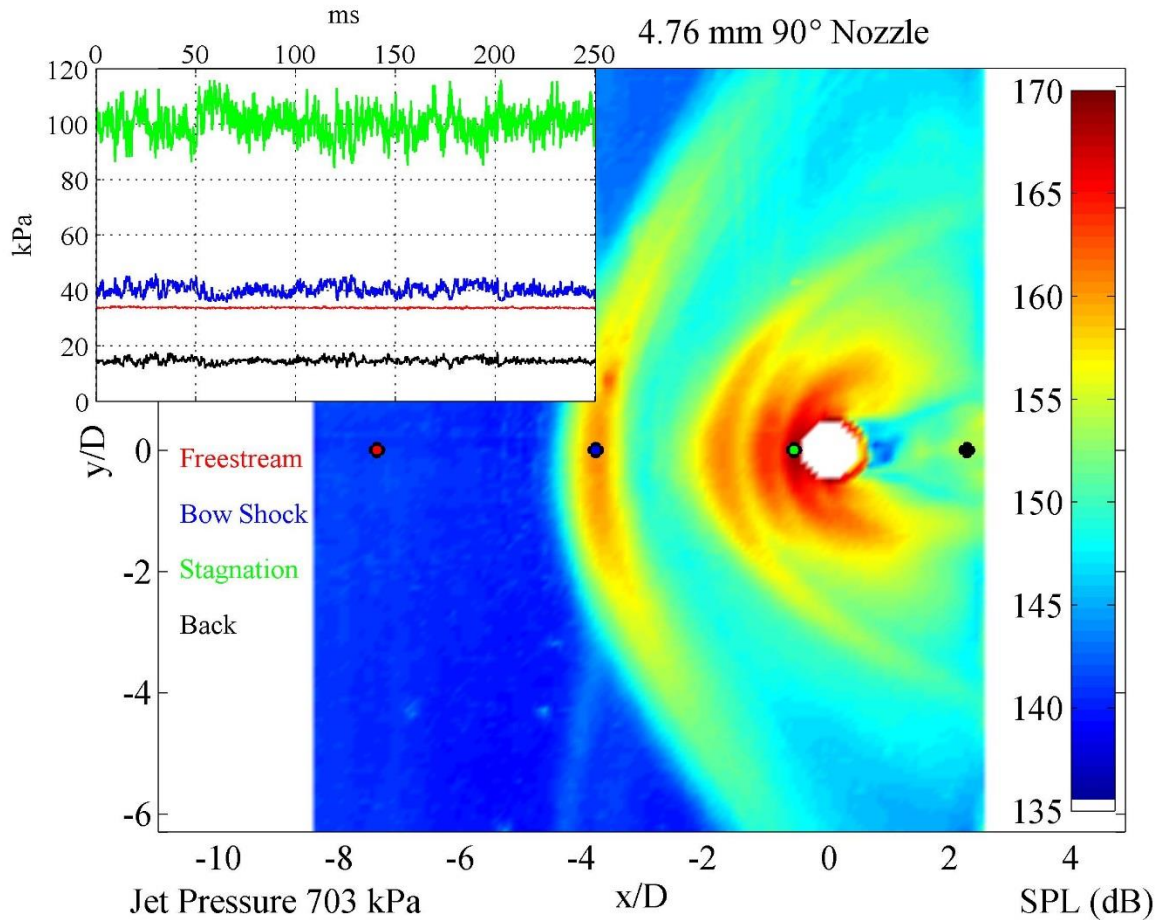


**Figure 13: Pressure fluctuations and time history at the four indicated locations for the 4.76–mm-diam., 90° injector block operating at  $P_{inj} = 703\text{-kPa}$ .**

The amplitude of the pressure fluctuations for the 4.76-mm-diameter, 90° nozzle was computed for each of the jet injection pressures and converted to SPL. Images, similar to Figure 13, were prepared at each test condition and revealed a similar structure. The major source of pressure fluctuations in the flow is associated with the bow shock, the stagnation zone, and the junction vortex. The SPL along the centerline of the flow is plotted for each injection pressure in Figure 14. At each injection pressure, the pressure fluctuations are largest just upstream of the jet. There is a secondary peak in the pressure fluctuations upstream of the jet at about the same location as the pressure peak from the junction vortex seen in Figure 7. In both figures, the location of the peak (mean or fluctuation pressure) moves closer to the jet as the injection pressure is decreased. It is noted that the amplitude of the mean pressure peak associated with the junction vortex is relatively constant while the fluctuating peak is larger at the highest injection pressure, lowest at the low injection pressure, and relatively constant in between.

It is noted that the minimum SPL exhibited in Figure 13 and Figure 14 is on the order of 140 dB (200 Pa). This does not necessarily correspond to the minimum level of pressure fluctuations in the tunnel. It may represent a noise floor for the PSP measurement for this experimental setup. An estimation of the minimum pressure fluctuation that can be detected based on the assumption that shot noise is the dominant noise source indicates a noise floor of about 170 Pa for this experimental setup and data processing scheme. This is close to the 200 Pa noise floor indicated in Figure 13 and Figure 14, and therefore, it is concluded that the noise floor is related to the measurement system, not the actual tunnel environment.

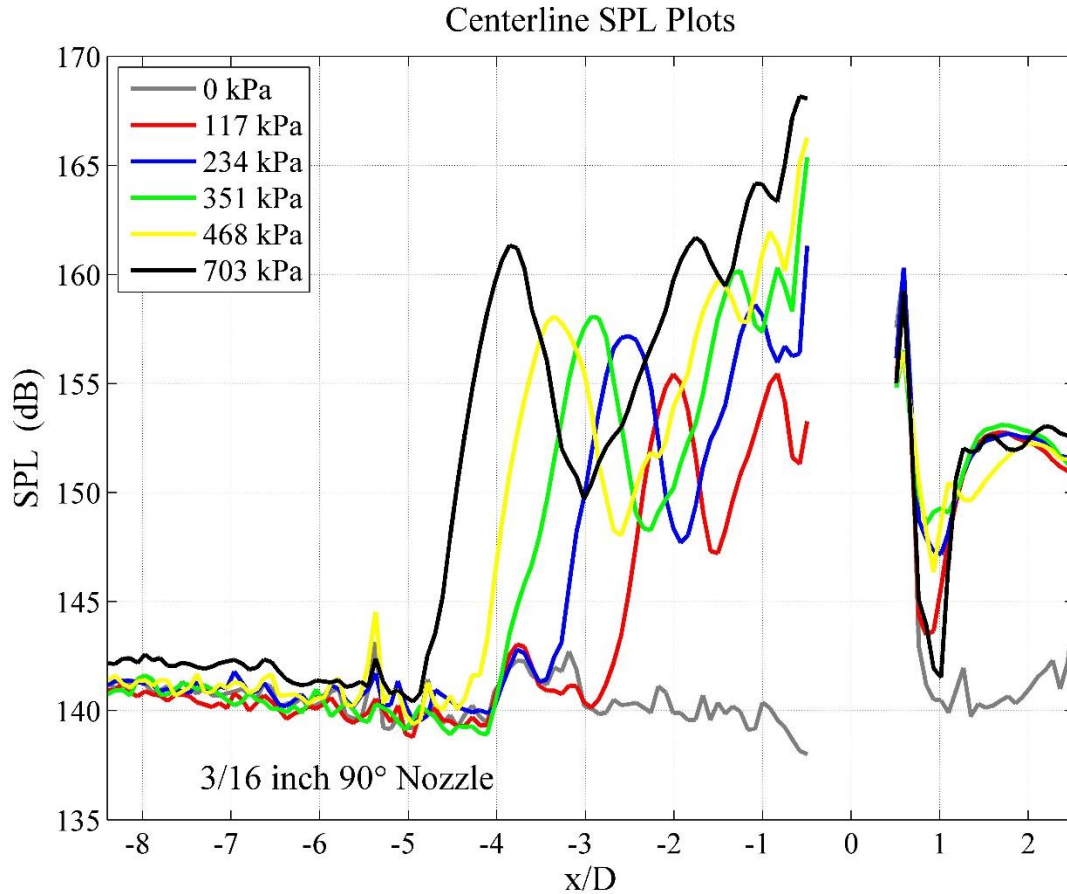


**Figure 14: Pressure fluctuations along jet centerline for the 4.76-mm-diam., 90° injector block operating at several injection pressures.**

A similar pressure fluctuation analysis was performed on the 4.76-mm-diameter, 30° nozzle, and an example of the resulting pressure fluctuations, presented as SPL, is shown in Figure 15. The overall structure is similar to those in Figure 14; however, the amplitude of the pressure fluctuations are somewhat smaller. The low-noise freestream region is still evident upstream of the bow shock, while the bow shock and region downstream of the jet comprise the regions with high pressure fluctuations. The stagnation zone upstream of the jet is smaller and the amplitude of the pressure fluctuations is smaller than those in the bow shock, unlike with the 90° injector (Figure 14). This is likely due to the inclined injection scheme, which presents less of an obstruction to the flow.

The SPL along the centerline for each injection condition is shown in the top left corner of Figure 15. The location of the peak pressure fluctuations associated with the bow shock and the location of peak pressure fluctuations in the stagnation zone move closer to the jet as the injection pressure decreases. The amplitude of the pressure fluctuations increases as the jet injection pressure increases at both locations, with the exception of the bow shock at the 703 kPa injection pressure. In this case, the SPL amplitude decreases, in contrast to the 90° injection case (Figure 14).

Data analysis of the fast PSP data is not limited to simple mean and fluctuating pressure maps. The time history of the data at each pixel can be analyzed spectrally to present frequency content of the flow as a function of spatial location, or cross-correlated<sup>16</sup> to reveal regions of the flow that are correlated. As a demonstration, the power spectrum of the time history data presented in Figure 13 can be computed to investigate the frequency content of the flow at these four locations, as shown in Figure 16. There are no clear peaks in any of the spectra, suggesting that there is no fundamental frequency content to this flow. The freestream data contains no significant pressure fluctuations, and the SPL data flattens out to around 105-dB above 250 Hz. The spectra from the data behind the jet and at the bow shock have very similar spectral content with the amplitude of the SPL behind the jet being about 5 dB lower than at the

bow shock. The power spectrum of the data near the bow shock and behind the jet both decay to a value near the freestream data by about 2 kHz. The most intense pressure fluctuations are located near the stagnation point.

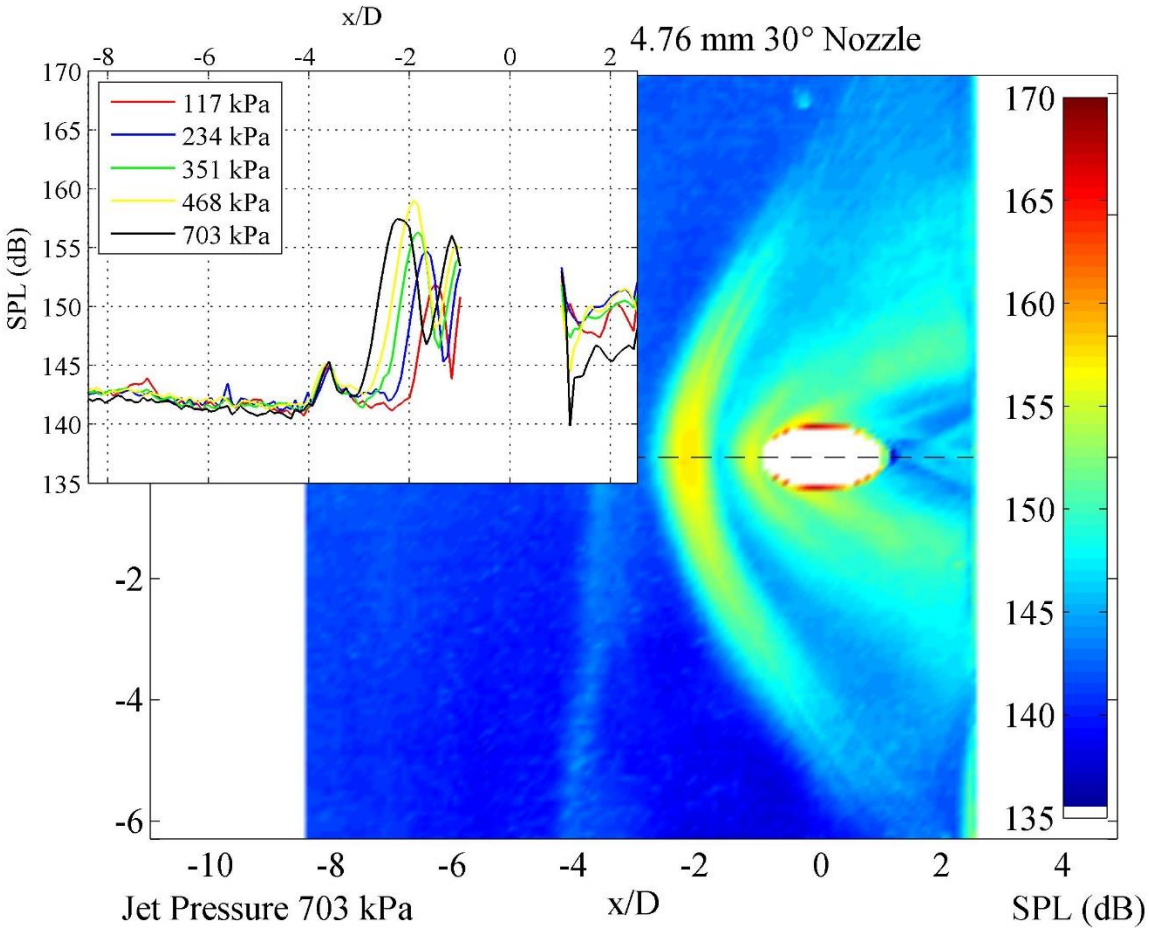


**Figure 15: Pressure fluctuations for the 4.76–mm-diam., 30° injector block operating at  $P_{inj} = 703\text{-kPa}$ .**

Of course, it is possible that the bandwidth offered by the 7 kHz data acquisition (3.5 kHz) may not fully resolve the spectra of the flow in the stagnation zone. To better evaluate the frequency content of the flow, a 4000 image data set was acquired with a reduced field of view at a rate of 25 kHz. The spectra at the bow shock and stagnation zone locations were thus computed and are shown in Figure 16. The spectra match the 7 kHz data to within a few dB, and the spectra at both locations continue to roll off with no peaks evident below 12.5 kHz. It is concluded that the 7 kHz data effectively resolves the flow at all locations other than near the stagnation zone, and at that location, it is only missing low amplitude pressure fluctuations.

It is recognized that the data and analysis presented in Figure 13 and Figure 16 are identical to the data and analysis that can be performed with a few traditional fast pressure transducers. The major advantage of the current system is that there are over 26,000 transducers available for the analysis. This data can be extracted at each pixel and analyzed to produce maps of mean and fluctuating pressure (Figure 13 and Figure 15), to analyze the frequency content of the flow with high spatial resolution, or to investigate relationships between different regions of the flow using correlation analysis.

The time series data from each of the test conditions was processed spectrally at each pixel to produce a map of the amplitude of the pressure fluctuations at each frequency. The 5,000 sample data set (4.76 mm diam. 90° nozzle at 703 kPa injection pressure) allowed more averaging, and therefore, produced data with the best signal-to-noise ratio. Maps of the resulting pressure fluctuations at several frequency bins is shown in Figure 17. Each frequency bin spans 27 Hz and is centered on the frequency indicated above the map.

In the lowest frequency bin (~27 Hz), the pressure fluctuations are strong throughout the bow shock and near stagnation zones in front of the jet. The structure of the bow shock and the horseshoe vortex is consistent with the broadband pressure fluctuation data in Figure 13. The amplitudes of the pressure fluctuations upstream of the jet/shock structure are relatively uniform without any noticeable spatial distribution. At the next frequency bin (~81 Hz), the pressure fluctuations in the freestream zone have dropped noticeably, and the strong pressure fluctuations in the bow shock and stagnation zones are focused near the major axis of the jet flow. Between 200 Hz and 300 Hz, a set of weak expansion fans appear in the flow. These expansion fans can be identified in the broadband data, and at other frequencies; however, they seem to be stronger relative to other components of the flow in this frequency range. At higher frequencies the amplitude of the fluctuations continues to drop, while some complex node structures begin to appear. At 670 Hz, for example, a bifurcated node structure appears in the stagnation zone and through the horseshoe vortex. Interestingly, these node structures are only present at this frequency bin. At frequencies above about 2 kHz the only significant pressure fluctuations are associated with the stagnation zone in front of the jet. A sequence of several hundred of these maps can be combined into a movie, thus allowing the frequency content of the flow to be visualized.

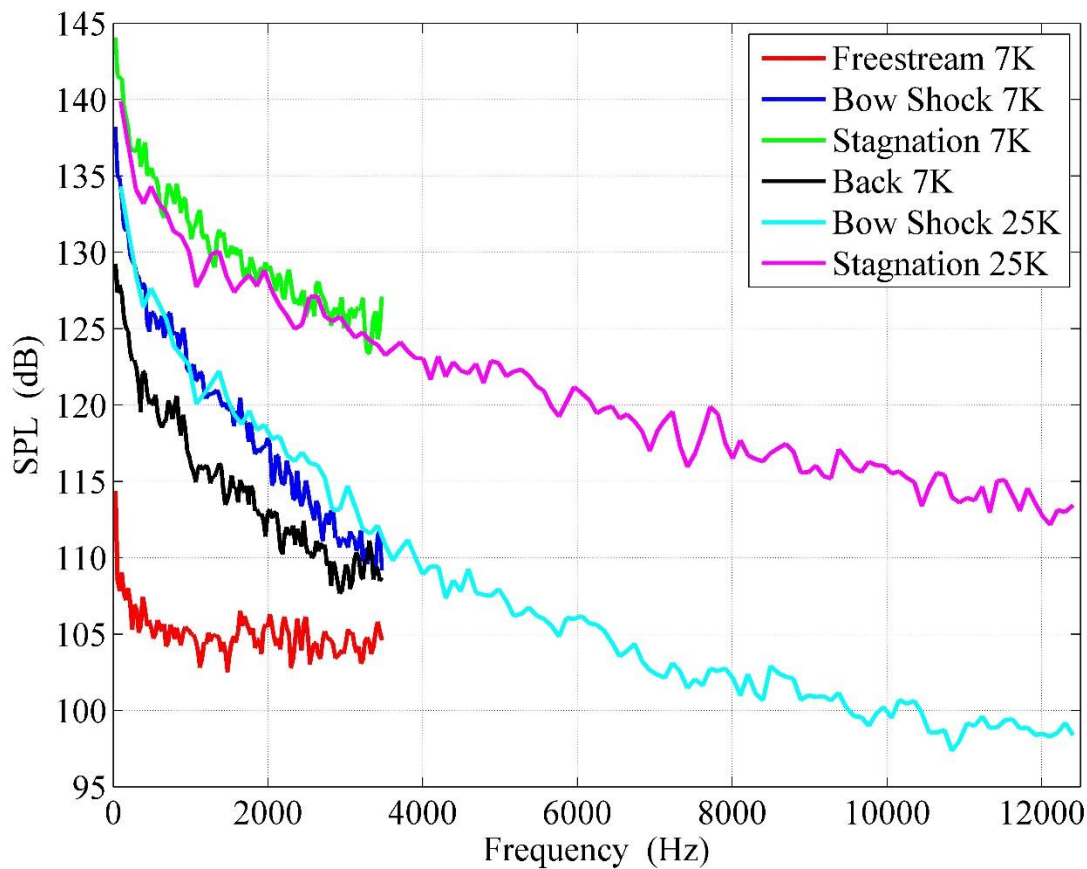
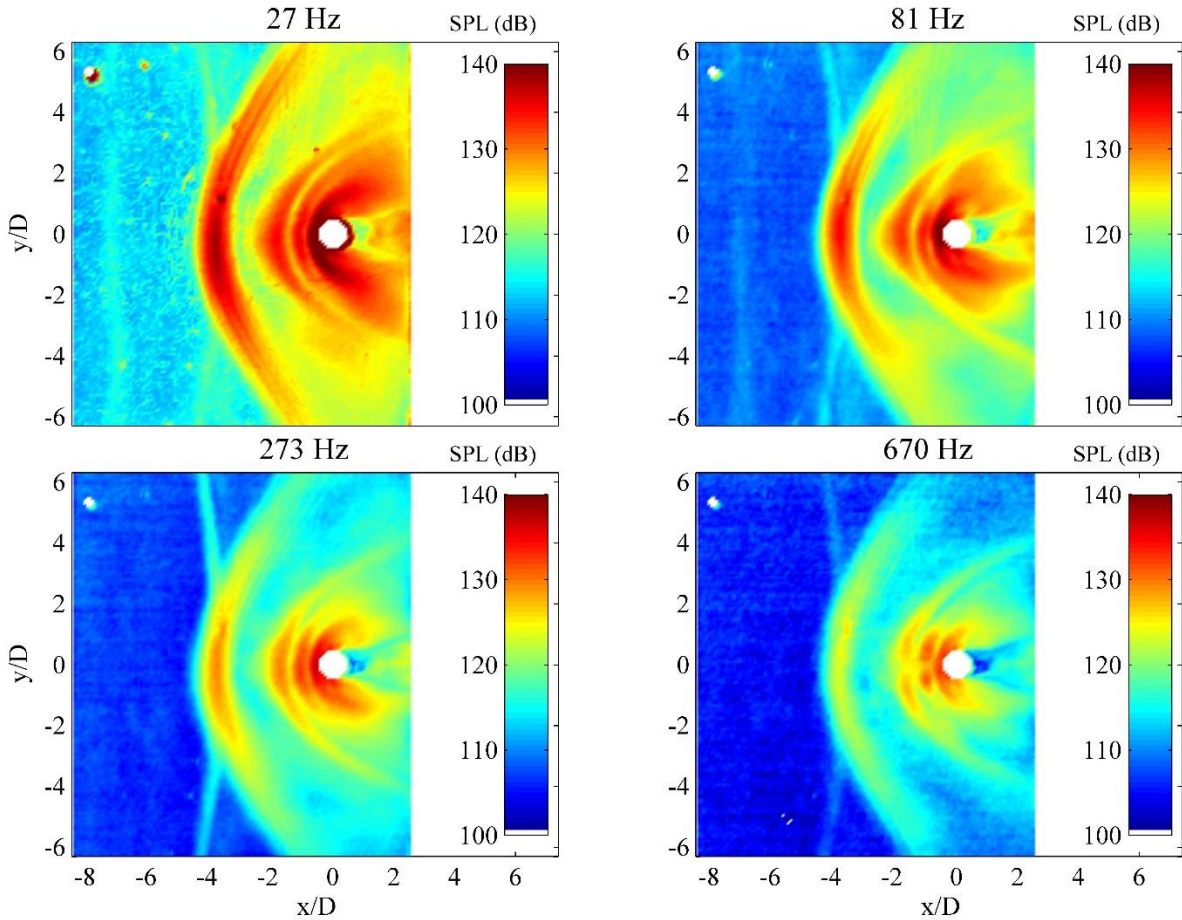


Figure 16: Amplitude of the power spectrum from the fast PSP pressure data presented in Figure 13.



**Figure 17: Map of the power spectrum amplitude at several frequencies for the 4.76-mm-diam., 90° injector block operating at  $P_{inj} = 703$ -kPa.**

It is clear from data such as those in Figure 13 and Figure 15 that specific regions of the flow contain significant pressure fluctuations. It is reasonable to assume that there may be some regions of the flow that influence one another; for example, the pressure fluctuations in the stagnation zone may drive the unsteadiness of the flow behind the jet or in the bow shock. It is possible to study the relationship between the pressure fluctuations at the different locations by computing a correlation coefficient between a particular control point in the flow and the remaining flowfield. The correlation coefficient for six control points, one in the freestream, one in the bow shock, one in the stagnation zone, and three points spread laterally behind the jet, was computed for the 4.76-mm-diameter, 90° nozzle operating at 703 kPa injection pressure. The resulting map of the correlation coefficient for each of these control points is shown in Figure 18.

The correlation maps are scaled from 1 to -1, with a value of 1 indicating a strong correlation (pressure rises as control point pressure rises), a value of -1 indicating a strong negative correlation (pressure falls as control point pressure rises), and a value of 0 indicating no correlation. Not surprisingly, the data indicate that the freestream has very little influence on the jet/bow shock structure. The pressure fluctuations in the stagnation zone, which has the strongest pressure fluctuations with the largest bandwidth, correlate mildly to those at the nose of the bow shock and behind the jet. The strongest correlation is between the pressure fluctuations near the bow shock and those in the low pressure zone behind the jet. In this case, there is both a strong positive (nose of the bow shock) and negative (boundary of the bow shock) correlation. The correlation maps from the two control points that are behind the jet but off axis also show a strong asymmetric correlation with the bow shock structure. It is suggested that as the magnitude and position of the low-pressure zone behind the jet fluctuate, the backpressure on the upstream flow is effectively changed. This will directly impact the location and magnitude of the upstream bow shock. As the low-pressure zone

behind the jet flaps side to side, the bow shock bow shock responds generating the asymmetric pattern seen in Figure 18.

A similar analysis was performed on the 7.94-mm-diameter, 90° nozzle operating at 703 kPa injection pressure. Theoretically, the only difference in these test conditions is the Reynolds number, and therefore, similar results are expected. The correlation maps and corresponding control point locations are shown in Figure 19. The field of view of the fast PSP system was constant while the jet diameter increased, and therefore, it is not possible to match all of the control points. The points that do match, the bow shock, the stagnation zone, and behind the jet, result in similar correlation maps. The stagnation zones have a strong negative correlation to the flow around the front of the jet and in the nose of the horseshoe vortex. The bow shock correlates with the flow behind the jet. It is also noted that there are a series of sharp bow waves, which are assumed to be the lambda shocks seen in Figure 12, that are moving in phase with the pressure behind the jet. While these waves are present in Figure 18, there appear to be more of them, and they extend further upstream in Figure 19. Finally, the control points behind the jet, and to each side of the jet, produce very similar correlation maps in Figure 18 and Figure 19, specifically the asymmetric nature of the flow. Data such as that presented in Figure 18 could be useful for receptivity studies in a variety of flows, as well as for locating point sensors for closed loop flow control.

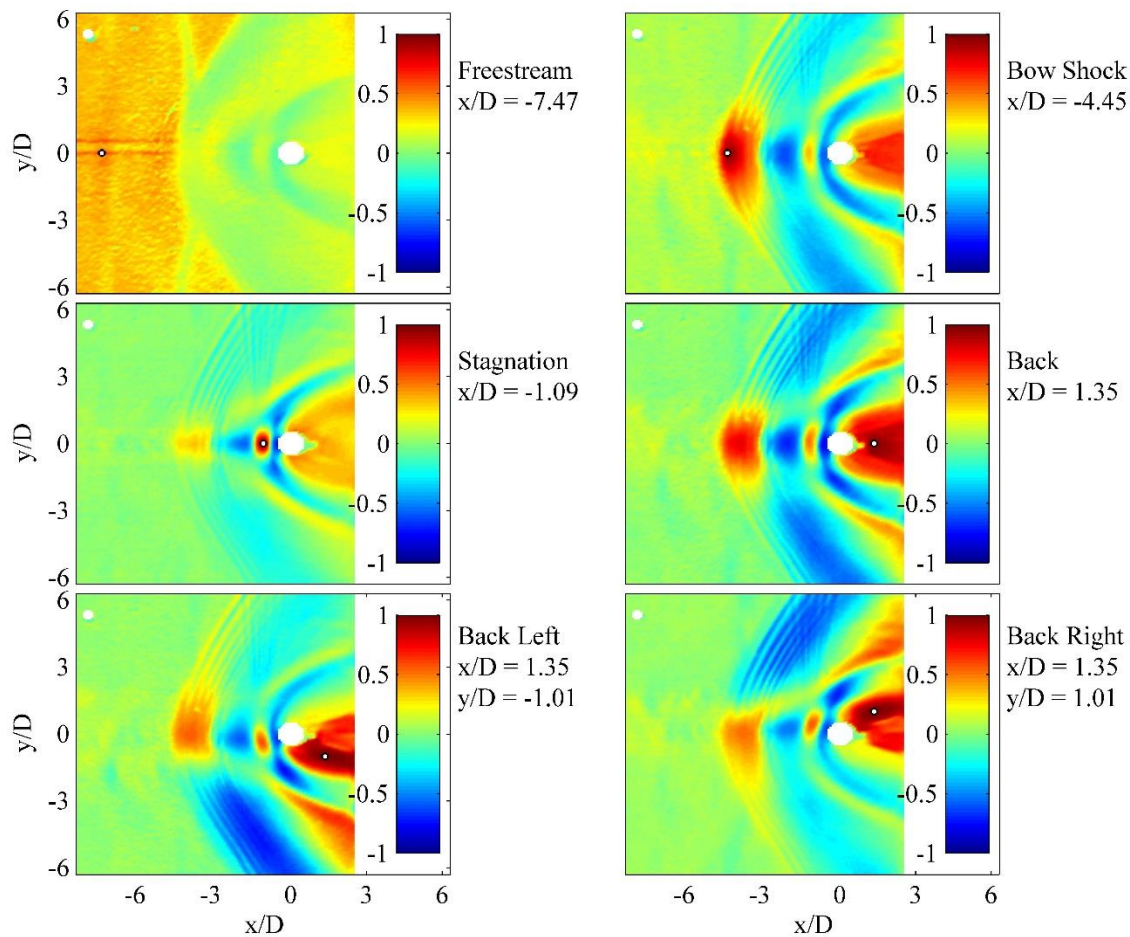


**Figure 18: Maps of the correlation coefficient for the 4.76–mm-diam., 90° injector block operating at  $P_{inj} = 703$ -kPa.**

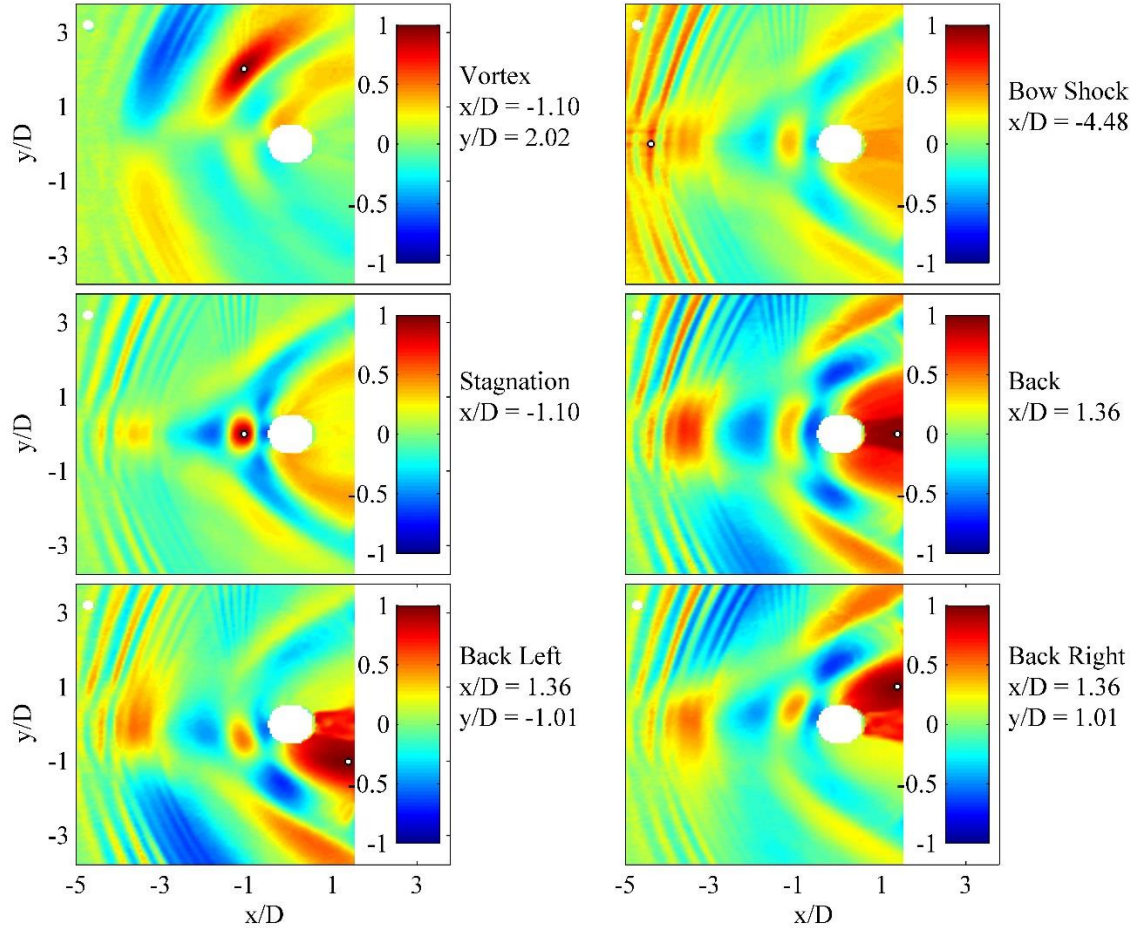


**Figure 19: Maps of the correlation coefficient for the 7.94–mm-diam., 90° injector block operating at  $P_{inj} = 703$ -kPa.**

#### IV. Conclusions

Pressure-Sensitive Paint (PS) has been used to study the mean and unsteady pressure distribution on a surface near a jet injection site in a Mach-2 channel flow. The experimental study included four injection blocks: two 90° (normal) jets and two 30° jets, with injector diameters of 4.76 and 7.94 mm. The tunnel stagnation pressure was 234 kPa and the jet was operated at jet-to-freestream momentum flux ratios of 0.5, 1.0, 1.5, 2.0 and 3.0. Mean measurements of pressure were acquired using a traditional binary PSP system. This system was comprised of binary FIB PSP, LM2X-400 LEDs, and a PCO.1600 camera with a filter wheel. Unsteady measurements were acquired at 7-kHz and 25-kHz using a fast responding PSP, an LM2XX-400 LED, and a Photron SA-5 CMOS camera. The binary PSP results were utilized as an *in-situ* calibration tool for the fast PSP data. The high-spatial-resolution pressure measurements indicate that normal injection (injection angle of 90°) of the jet results in a flow that is similar to a strut-endwall configuration. There is a strong bow shock well upstream of the jet, a stagnation zone in front of the jet, and a horseshoe vortex upstream of the stagnation zone. As the injection pressure is increased, the scale of the structures is expanded, but the basic structure of the flow is unchanged. Injector blocks with an injection angle of 30° were also studied. In this case, the bow shock was weaker, and there was no strong stagnation zone or horseshoe vortex. The surface pressure near the injectors was also interrogated using a fast PSP system. Full frame images ( $1k \times 1k$ ) were acquired at 7 kHz; images with a reduced spatial resolution ( $512 \times 512$  pixels) were acquired at 25 kHz. The time-averaged pressure data from the fast PSP system compared favorably to PSP data acquired using the binary FIB system. The unsteady pressure data clearly resolves structures not present in the mean pressure data. These structures include multiple lambda shocks upstream of a strong bow shock, high frequency perturbations in the location of these shocks, and significant deformations of the bow shock structure. Time series data can be extracted at each image pixel, and the spectral content

and phase relationship of the flow can be investigated spatially. This type of spectral map can be created using arrays of fast pressure transducers; here, however, we present data representing an array of over 26,000 fast pressure transducers. Finally, the fast PSP can be used to create maps of the correlation coefficient between specific reference points and the remaining flow. These correlation maps suggest that it is the low pressure region of the flow behind the jet that has the strongest impact on the unsteadiness of the bow shock.

### Acknowledgments

This work was supported by AFRL/RQH and by the Air Force Office of Scientific Research (AFOSR). The authors would like to thank the staff of Test Cell 19 for their support of this test.

### References

---

- <sup>1</sup> F Genin and S Menon, "Dynamics of sonic jet injection into supersonic crossflow" *J. of Turbulence* vol. 11, No. 4, pp. 1-30, (2010)
- <sup>2</sup> JA Boles, C Jung-II, JR Edwards, and RA Baurle, "Simulations of High-Speed Internal Flows using LES/RANS Models," AIAA Paper 2009-1324, (2009)
- <sup>3</sup> D Peterson and G Candler, "Hybrid Reynolds-averaged and large-eddy simulation of normal injection into a supersonic crossflow", *J. Prop. Power* vol. 26, no. 3, pp. 533-544 (2010)
- <sup>4</sup> A Ferrante, G Matheou,, and PE Dimotakis, "LES of an Inclined Sonic Jet into a Turbulent Crossflow at Mach 3.6", In preparation
- <sup>5</sup> KC Lin, M Ryan, CD Carter, MR Gruber, and C Raffoul, "Raman Scattering Measurements of Gaseous Ethylene Jets in Mach 2 Supersonic Crossflow", vol. 26, no. 3, pp. 503-513, (2010)
- <sup>6</sup> T Liu and JP Sullivan, "Pressure and Temperature Sensitive Paints", Springer-Verlag, Berlin (2004)
- <sup>7</sup> JW Gregory, K Asai, M Kameda, T Liu, and JP Sullivan, "A Review of Pressure-Sensitive Paint for High Speed and Unsteady Aerodynamics," *Journal of Aerospace Engineering*, vol. 222, No. 2, pp. 249-290 (2008)
- <sup>8</sup> A Bykov, S Fonov, V Mosharov, A Orlov, V Pesetsky, V Radchenko, "Study Result for the Application of Two-component PSP Technology to Aerodynamic Experiment", AGARD (1997)
- <sup>9</sup> G Khalil, C Costin, J Crafton, G Jones, S Grenoble, M Gouterman, J Callis, L Dalton "Dual Luminophor Pressure Sensitive Paint I: Ratio of Reference to Sensor Giving a Small Temperature Dependence" *Sensors and Actuators B*, vol. 97, n 1, pp. 13-21
- <sup>10</sup> J Crafton, S Fonov, E Jones, V Fonov, L Goss, "Simultaneous Measurements of Pressure and Deformation on a UCAV in the SARL", AIAA-2005-1028
- <sup>11</sup> A Scroggin, EB Slamovich, JW Crafton, N Lachendro, JP and Sullivan, "Porous polymer/ceramic composites for luminescence-based temperature and pressure measurement", *Proceedings of the Materials Research Society Symposium*, 1999, vol. 560, pp. 347-352
- <sup>12</sup> JW Gregory, JP Sullivan, G Raman, and S Raghu, "Characterization of the Microfluidic Oscillator," *AIAA Journal*, vol. 45, No. 3, pp. 568-576, (2007)
- <sup>13</sup> S Fonov, RH Engler, C Klein, S Mihailov, VE Mosharov, VP Kulesh, VN Radchenko, and E Schairer, "Pressure sensitive paint for oscillating pressure fields measurements", 18th ICIASF, pp. 24.1-24.4, (1999)
- <sup>14</sup> M Kameda, T Tabei, K Nakakita, H Sakaue, and K Asai, "Image measurements of unsteady pressure fluctuation by a pressure-sensitive coating on porous anodized aluminum" *Meas. Sci. Technol.*, vol. 16, No. 12, pp-2517-2524 (2005)
- <sup>15</sup> K Nakakita, , "Unsteady pressure distribution measurement around 2D-cylinders using pressure-sensitive paint", AIAA-2007-3819
- <sup>16</sup> MC Merienne, Y Le Sant, F Lebrun, B Deleglise, D Sonnet, "Transonic Buffeting Investigation using Unsteady Pressure-Sensitive Paint in a Large Wind Tunnel", AIAA-2013-1136